

Banner appropriate to article type will appear here in typeset article

# Direct numerical simulations of turbulent mixing driven by the Faraday instability in rotating miscible fluids.

Narinder Singh<sup>1</sup> and Anikesh Pal<sup>1</sup>†

<sup>1</sup>Department of Mechanical Engineering, Indian Institute of Technology Kanpur, Kanpur 208016, U.P., India

(Received xx; revised xx; accepted xx)

The effect of the rotation on the turbulent mixing of two miscible fluids of small contrasting density, induced by Faraday instability, is investigated using direct numerical simulations (DNS). We quantify the irreversible mixing which depicts the conversion of the available potential energy (APE) to the background potential energy (BPE) through irreversible mixing rate  $\mathcal{M}$ . We demonstrate that at lower forcing amplitudes, the turbulent kinetic energy (*t.k.e.*) increases with an increase in the Coriolis frequency  $f$  till  $(f/\omega)^2 < 0.25$ , where  $\omega$  is the forcing frequency, during the sub-harmonic instability phase. This enhancement of *t.k.e.* is attributed to the excitement of more unstable modes. The irreversible mixing sustains for an extended period with increasing  $(f/\omega)^2$  till 0.25 owing to the prolonged sub-harmonic instability phase and eventually ceases with instability saturation. When  $(f/\omega)^2 > 0.25$ , the Coriolis force significantly delays the onset of the sub-harmonic instabilities. The strong rotational effects result in lower turbulence because the bulk of the APE expends to BPE, decreasing APE that converts back to *t.k.e.* reservoir for  $(f/\omega)^2 > 0.25$ . Therefore, in the subsequent oscillation, the *t.k.e.* available to contribute to the external energy input from periodic forcing is small. Since the instability never saturates for  $(f/\omega)^2 > 0.25$ , conversion of APE to BPE via  $\mathcal{M}$  continues, and we find prolonged irreversible mixing. At higher forcing amplitudes, the instability delaying effect of rotation is negligible, and the turbulence is less intense and short-lived. Therefore, the irreversible mixing phenomenon also ends quickly for  $(f/\omega)^2 < 0.25$ . However, when  $(f/\omega)^2 > 0.25$ , a continuous irreversible mixing is observed. We also examine the mixing efficiency in terms of  $\mathcal{M}$  and find that the mixing is efficient at lower forcing amplitudes and rotation rates of  $(f/\omega)^2 > 0.25$  because the major portion of APE expends to BPE.

**Key words:**

---

† Email address for correspondence: pala@iitk.ac.in

## 1. Introduction

The Faraday instability (Faraday 1831) describes the generation of standing wave patterns at the interface of two immiscible fluids subjected to vertical periodic vibration. However, in a stably stratified two-layer miscible fluid system, these standing waves become highly disorganized above a certain forcing amplitude and start to interact with each other resulting in the mixing of fluids which eventually saturates (Zoueshtiagh *et al.* 2009; Amiroudine *et al.* 2012; Diwakar *et al.* 2015). Gréa & Adou (2018); Briard *et al.* (2019) studied the onset and saturation of turbulent mixing owing to Faraday instability in fluids of small contrasting density for a wide range of parameters using theoretical models and DNS. They demonstrated that the diffuse interface begins to oscillate with small amplitude in the harmonic instability phase, followed by the rapid growth and development of a turbulent mixing zone in the sub-harmonic instability phase. However, owing to the saturation of the instability, the turbulent mixing cannot be sustained for long. They also estimated the final size of the mixing zone analytically as follows:

$$L_{sat} = \frac{2\mathcal{A}g_0}{\omega^2} (2F + 4), \quad (1.1)$$

where  $L_{sat}$  is the final asymptotic size of the mixing zone (defined later) in saturation state,  $\mathcal{A} = (\rho_1 - \rho_2) / (\rho_1 + \rho_2)$  is the Atwood number expressing the density contrast between heavy fluid ( $\rho_1$ ) and light fluid ( $\rho_2$ ),  $g_0$  is the mean acceleration,  $F$  is the oscillation amplitude and  $\omega$  is the forcing frequency. Briard *et al.* (2019) numerically presented the quantification of irreversible mixing associated with turbulent mixing by partitioning the total potential energy (PE) into background potential energy (BPE) and available potential energy (APE). They reported that the BPE signifying the measure of irreversible mixing increases during the onset of sub-harmonic instability. The APE, which represents the fraction of the total PE that can be transferred to BPE through irreversible mixing, peaks at saturation and is partially released in the flow as BPE. This results in more irreversible mixing, which causes the numerically computed final mixing zone size  $L$  to exceed the analytically predicted  $L_{sat}$  1.1. Briard *et al.* (2020) performed a linear stability analysis accounting for the vertical inhomogeneity of the background density profile and viscous dissipation to predict the onset of the Faraday instability, either from a sharp or a diffuse interface and its eventual saturated state. Further experiments were carried out by Briard *et al.* (2020); Cavalier *et al.* (2022) using fresh and salty water to explore the dynamics of turbulent mixing, and DNS and theoretical predictions confirmed their findings. They found that when the instability is triggered, a natural wavelength appears at the interface between the two fluids. With the increase in amplitude, well-defined structures form that break due to the destabilization process at the nodes to produce turbulent mixing. Turbulence is eventually inhibited by instability saturation, and the final size of the mixing layer is consistent with the analytically predicted  $L_{sat}$ . Recently, Singh & Pal (2022) presented a theoretical analysis of Faraday instability in miscible fluids under the effect of rotation and corroborated their findings with DNS. They reported that rotational effects delay the onset of the sub-harmonic instability at lower forcing amplitudes ( $F$ ), owing to the presence of a stable region between the harmonic to sub-harmonic transition and before the onset of the sub-harmonic instabilities. In the stable region, the mixing layer grows due to diffusion. However, with an increase in  $F$ , the instability delaying effect of rotation diminishes due to the increasing area of all the unstable regions in the 3D stability diagram, resulting in the majority of excited modes being unstable. They concluded that the instability saturates for  $(f/\omega)^2 < 0.25$  and the mixing zone size asymptotes. However, for  $(f/\omega)^2 \geq 0.25$ , the instability does not saturate, and the mixing zone size continues to grow.

These studies have demonstrated the potential of the Faraday instability to promote mixing in stably stratified fluids depending on the various parameters, such as frequency and amplitude of the vibrations and the strength of the initial stratification. Understanding the turbulent diapycnal mixing in stably stratified ocean interior is important as it plays a major role in the global overturning circulation that transports water mass, heat, nutrients, and other biochemical substances (Wunsch & Ferrari 2004; Talley *et al.* 2016). The Faraday instability provides a framework to understand these flows and can help to elucidate the underlying physical processes that govern mixing in the oceanographic flows. The Earth's rotation significantly affects the dynamics of diapycnal mixing processes in the thermocline, as reported in studies by Noh & Long (1990); Fernando (1991) and Fleury *et al.* (1991). For example,  $N/f \approx 4.67$ , where  $N$  is the Brunt Väisälä frequency, in the abyssal southern ocean at mid-latitude (Nikurashin *et al.* 2013; Rosenberg *et al.* 2015). Modeling the properties of turbulence and the associated irreversible mixing, where external forcing, Earth's rotation and stratification play a central role, is a major challenge in geophysical fluid dynamics. Motivated by the turbulent mixing in the oceanic flows, we aim to quantify the irreversible mixing and mixing efficiencies associated with the turbulent mixing driven by the time-periodic accelerations in rotating miscible fluids using DNS. In the present investigations, we follow the framework of Winters *et al.* (1995), which was used to study the energetics of shear-induced mixing of stably stratified fluids by partitioning the total PE into BPE and APE. It is important to note that the Faraday instability drives the turbulent mixing, which induces small-scale turbulence and vertical motions that can enhance the mixing of stably stratified fluids. However, the turbulent mixing in stratified shear flows is typically driven by the Kelvin-Helmholtz instability resulting from velocity shear across the density gradient. As a result, the dynamics of the mixing layer differ between these two scenarios. Here, we focus on how the rotation affects the formation and subsequent breakdown of the structures on the diffuse interface to produce turbulence, irreversible mixing, and mixing efficiencies. To address these aims, the paper is organized as follows. In §2, we discuss the governing equations with boundary equations and the set-up for the simulations and briefly explain the theoretical framework for linear stability analysis developed in Singh & Pal (2022). We then discuss the predictions of the linear stability analysis and the numerical results in §3. Finally, we conclude in §4.

## 2. Methods

### 2.1. Governing equations

The two-layer miscible fluid system with small density contrast is considered here, which is driven by vertical periodic oscillations of acceleration  $g(t) = g_0(1 + F \cos(\omega t))$ . We consider the density of the mixture to be a linearly varying function of mass concentration such that the lighter fluid with concentration  $C(\rho_2) = 0$  is placed above the denser fluid with  $C(\rho_1) = 1$  in a rectangular domain. The unsteady incompressible flow with Boussinesq approximation is governed by the three-dimensional conservation equations for mass, momentum, and concentration field under vertically periodic forcing  $g(t)$ , in the form (Singh & Pal 2022)

$$\nabla \cdot \mathbf{U} = 0, \quad (2.1a)$$

$$\frac{\partial \mathbf{U}}{\partial t} + \mathbf{U} \cdot \nabla \mathbf{U} = -\nabla P - f \hat{k} \times \mathbf{U} + \nu \nabla^2 \mathbf{U} - 2\mathcal{A}Cg(t)\hat{k}, \quad (2.1b)$$

$$\frac{\partial C}{\partial t} + \mathbf{U} \cdot \nabla C = \kappa \nabla^2 C. \quad (2.1c)$$

Here,  $\mathbf{U}$  denotes the velocity vector with components  $(U_1, U_2, U_3)$  in the horizontal  $x_1, x_2$  and vertical  $x_3$  directions respectively,  $P$  is the pressure deviation from the hydrostatic background state,  $\nu$  ( $\text{m}^2 \text{s}^{-1}$ ) is the kinematic viscosity, and  $\kappa$  ( $\text{m}^2 \text{s}^{-1}$ ) is the diffusion coefficient. The Reynolds decomposition is performed to decompose a variable, say  $B$ , into its horizontally averaged mean component  $\langle B \rangle_H$  and fluctuating component  $b$ , given by

$$B(x_1, x_2, x_3, t) = \langle B \rangle_H(x_3, t) + b(x_1, x_2, x_3, t), \quad (2.2a)$$

$$\langle B \rangle_H(x_3, t) = \frac{1}{l_{x_1} l_{x_2}} \int_{-l_{x_1}/2}^{+l_{x_1}/2} \int_{-l_{x_2}/2}^{+l_{x_2}/2} B(x_1, x_2, x_3, t) dx_1 dx_2. \quad (2.2b)$$

Here,  $\langle \rangle_H$  denotes the horizontal average in the homogeneous directions  $x_1$  and  $x_2$ ,  $\langle b \rangle_H = 0$ , and  $l_{x_1}, l_{x_2}$  are the domain lengths in the  $x_1$  and  $x_2$  directions. The mixing zone size- $L$  is computed from mean concentration profile  $\langle C \rangle_H$  (Andrews & Spalding 1990) as  $L = 6 \int_{-\infty}^{+\infty} \langle C \rangle_H(x_3, t) (1 - \langle C \rangle_H(x_3, t)) dx_3$ . The stratification (or Brunt Väisälä) frequency is defined as

$$N = \sqrt{-2\mathcal{A}g_0 \frac{\partial \langle C \rangle_H}{\partial x_3}}, \quad (2.3)$$

where the vertical gradient of mean concentration approximated as  $\partial \langle C \rangle_H / \partial x_3 = -1/L$ .

## 2.2. Theoretical model

Singh & Pal (2022) presents the details of the inviscid linear stability analysis of the Faraday instability in a rotating and vertically oscillating two-layer miscible fluid system. Here, we briefly discuss the origin of the derivation of the linearized governing equations (Mathieu equations) along with the assumptions. The equations for the fluctuating velocity  $\mathbf{u}(\mathbf{x}, t)$  and the concentration  $c(\mathbf{x}, t)$  fields are obtained by substituting the Reynolds decomposition 2.2a into the governing equations 2.1a, 2.1b and 2.1c, with mean velocity field  $\langle \mathbf{U} \rangle_H = 0$  and  $\langle \mathbf{u} \rangle_H = \langle c \rangle_H = \langle p \rangle_H = 0$ . The resulting equations are given as

$$\frac{\partial u_i}{\partial x_i} = 0, \quad (2.4a)$$

$$\frac{\partial u_i}{\partial t} + u_j \frac{\partial u_i}{\partial x_j} = -\frac{\partial p}{\partial x_i} + f \epsilon_{ij3} u_j \hat{e}_3 - 2\mathcal{A}g(t) c \delta_{i3} + \frac{\partial \langle u_i u_3 \rangle_H}{\partial x_3} + \nu \nabla^2 u_i, \quad (2.4b)$$

$$\frac{\partial c}{\partial t} + u_j \frac{\partial c}{\partial x_j} = -u_3 \frac{\partial \langle C \rangle_H}{\partial x_3} + \frac{\partial \langle u_3 c \rangle_H}{\partial x_3} + \kappa \nabla^2 c. \quad (2.4c)$$

We assume that the fluids are inviscid and the fluctuations in velocity and concentration are small. Therefore, the non-linear, the viscous, and the diffusion terms are neglected from the equations 2.4b and 2.4c. The concentration profile is assumed to be piecewise, i.e. constant in the bottom and upper pure (unmixed) fluids and linear in the mixing layer, with a vertical gradient of mean concentration  $\partial \langle C \rangle_H / \partial x_3 = 0$ , in the unmixed region and  $\partial \langle C \rangle_H / \partial x_3 = \text{constant}$ , in the mixed region. The detailed derivation of the linearized equations and their solution strategy is presented in Singh & Pal (2022). The final system of linearized equations (for  $N > f$ ), equivalent to a set of Mathieu equations, is given as

$$\frac{\partial^2 a}{\partial \tau^2} + \left( \frac{f^2 \cos^2(\theta)}{\omega^2} + \frac{N^2 \sin^2(\theta)}{\omega^2} (1 + F \cos(\tau)) \right) a = 0, \quad (2.5)$$

where,  $a$  represents the amplitude of the concentration field mode,  $\tau (= \omega t)$  is the non-dimensional time, and  $\theta$  is the angle between the vertical axis and the wavevector  $\mathbf{K}$  with

Case	$F$	$\omega$ (rad s <sup>-1</sup> )	$f$ (s <sup>-1</sup> )	$f/\omega$	$(f/\omega)^2$	$\eta_{cu}$
F075f/ $\omega$ 0	0.75	0.67	0	0	0	$\sim 0.495$
F075f/ $\omega$ 48	0.75	0.67	0.322	0.481	0.23	$\sim 0.363$
F075f/ $\omega$ 59	0.75	0.67	0.396	0.591	0.35	never saturate
F1f/ $\omega$ 0	1.0	0.7	0	0	0	$\sim 0.421$
F1f/ $\omega$ 48	1.0	0.7	0.338	0.482	0.23	$\sim 0.372$
F1f/ $\omega$ 59	1.0	0.7	0.414	0.591	0.35	never saturate
F2f/ $\omega$ 0	2.0	0.8	0	0	0	$\sim 0.392$
F2f/ $\omega$ 48	2.0	0.8	0.384	0.48	0.23	$\sim 0.366$
F2f/ $\omega$ 59	2.0	0.8	0.473	0.592	0.35	never saturate
F3f/ $\omega$ 0	3.0	0.9	0	0	0	$\sim 0.345$
F3f/ $\omega$ 48	3.0	0.9	0.432	0.48	0.23	$\sim 0.333$
F3f/ $\omega$ 59	3.0	0.9	0.532	0.592	0.35	never saturate

Table 1: Simulation parameters:  $\eta_{cu}$  is the cumulative mixing efficiency. For all cases we use Atwood number  $\mathcal{A} = 0.01$ , kinematic viscosity  $\nu = 1 \times 10^{-4} \text{ m}^2 \text{ s}^{-1}$ , diffusion coefficient  $\kappa = 1 \times 10^{-4} \text{ m}^2 \text{ s}^{-1}$ , and  $g_0 = 10 \text{ m s}^{-2}$  (Briard *et al.* 2019; Singh & Pal 2022).

components  $(k, l, m)$  in the  $x_1, x_2$  and  $x_3$  directions, respectively. The Floquet theory, which provides the solutions to linear differential equations with periodic coefficients, is utilized to solve a set of Mathieu equations 2.5. Details of solving the equation 2.5 using Floquet theory are presented in Appendix A. The solutions of the equation 2.5 can be stable or unstable which governs the stability of the system.

### 2.3. Simulation details

The governing equations 2.1a, 2.1b, and 2.1c are solved in a Cartesian coordinate system on a staggered grid using a finite difference method. The numerical algorithms are presented in Singh & Pal (2022). The numerical solver has been extensively validated and used for studies of rapidly rotating convection-driven dynamos (Naskar & Pal 2022a,b), rotating convection (Pal & Chalamalla 2020), and several stratified free-shear and wall-bounded turbulent flows (Brucker & Sarkar 2010; Pal *et al.* 2013; Pal & Sarkar 2015; Pal 2020). A sponge region is used near the top and bottom boundaries to control the spurious reflections from the disturbances propagating out of the domain, where damping functions gradually relax the velocities to their corresponding values at the boundaries. These damping functions are added on the right-hand side of the momentum equation 2.1b as explained in Brucker & Sarkar (2010). The sponge region is sufficiently far away from the mixing region such that it does not affect the dynamics of the mixing of fluids. We consider periodic boundary conditions for all variables in the  $x_1$  and  $x_2$  (horizontal) directions, whereas at the top and bottom walls ( $x_3$ ), no-slip boundary conditions for velocity vector  $\mathbf{U}$  and Neumann boundary conditions for  $C$  and pressure  $P$  are used. The initial concentration profile (Briard *et al.* 2019, 2020; Singh & Pal 2022) in the present simulations is given as

$$C(\mathbf{x}, t = 0) = \frac{1}{2} \left( 1 - \tanh \left( \frac{2x_3}{\delta} \right) \right), \quad (2.6)$$

where the parameter  $\delta$  is used to change the initial mixing zone size- $L_0$ .  $\delta = 0.035$  and corresponding  $L_0 = 0.096 \text{ m}$  is used across all simulations. Broadband fluctuations are imposed on the initial concentration profile 2.6 as reported in Singh & Pal (2022). The

domain size in the horizontal directions is  $l_{x_1} = l_{x_2} = 2\pi$  m, and in the vertical direction is  $l_{x_3} = 2H = 3.5\pi$  m which includes sponge region of thickness  $H_s = 0.64\pi$  m at top and bottom boundaries. We use uniform grids  $N_{x_1} = N_{x_2} = 512$  in the horizontal directions, while in the vertical direction  $x_3$ , non-uniform grids  $N_{x_3} = 512$  are used with clustering at the vertical centre region of thickness  $1.53\pi$  m with  $\Delta x_{3_{min}} = \Delta x_1 = \Delta x_2$ . Table 1 shows the key parameters for all simulation cases. We select three cases at each  $F$  depending on the value of  $f/\omega$ , where sub-harmonic instability saturates for  $f/\omega = 0$ , and  $0.48$  ( $(f/\omega)^2 < 0.25$ ) and never saturates for  $f/\omega = 0.59$  ( $(f/\omega)^2 \geq 0.25$ ) (Singh & Pal 2022). We refer each case with a unique name for example F075f/ω48, which indicates that  $F = 0.75$  and  $f/\omega = 0.48$ .

### 3. Results

#### 3.1. Linear stability analysis

Figure 1a shows the stability diagram at forcing amplitude  $F = 1$  in the  $(N/\omega)^2 - (f/\omega)^2$  parameter plane, obtained by solving the linearized governing equations (Mathieu equations) 2.5. The stable (white) regions are in between the unstable red (sub-harmonic) and cyan (harmonic) colored tongues. From the Floquet analysis (see Appendix A, Jordan & Smith (2007) and Singh & Pal (2022)), the solutions inside the first sub-harmonic tongue are periodic with period  $T = 4\pi$ . Therefore, the solutions grow and oscillate with frequency  $\omega/2$  because  $\cos(\tau)$ , where  $\tau = \omega t$ , in the equation (2.5) is periodic with  $T = 2\pi$  and frequency is  $2\pi/T = 1$ . However, the solutions grow in the second and third sub-harmonic tongues with frequencies of  $3\omega/2$  and  $5\omega/2$ , respectively. The solutions inside the first harmonic tongue are  $2\pi$  periodic and grow with frequency  $\omega$ , whereas, in the second and third harmonic tongues, the solutions grow with frequencies of  $2\omega$  and  $3\omega$ , respectively. The solutions that lie outside the harmonic and sub-harmonic instability tongues are stable. The contour curves for the growth rates ( $\sigma$ ), range from  $\sigma = 0.02$  to  $\sigma = 0.12$  with a step size of  $0.02$ , of the unstable  $\theta$ -modes inside the first leftmost sub-harmonic tongue are illustrated in figure 1b. The black curve corresponds to the neutral stability curve for  $\sigma = 0$ , which separates the regions of stable and unstable solutions. The inclined blue line (solid) segment in figure 1a demonstrates the possible frequencies ( $\in [(f/\omega)^2, (N_0/\omega)^2]$ ) that can be excited corresponding to an angle  $\theta \in [0, \pi/2]$ , for a given  $(f/\omega)^2 = 0.23$  and initial stratification condition  $(N_0/\omega)^2$  in the first harmonic tongue. This segment ranges from  $(f/\omega)^2$  (left end ( $\times$ ) at  $\theta = 0$ ) to  $(N_0/\omega)^2$  (right end ( $\times$ ) at  $\theta = \pi/2$ ). The unstable  $\theta$ -modes inside the sub-harmonic or harmonic tongues trigger the Faraday instability. This results in the growth of mixing zone size- $L$  and decrease of  $(N/\omega)^2$ , as indicated by the arrow directing to the left since  $(N/\omega)^2 = 2\mathcal{A}g_0/(L\omega^2) \propto 1/L$  from equation 2.3. Therefore, the condition for the occurrence of instabilities (Gréa & Adou 2018; Singh & Pal 2022) is defined based on the fact that if at least one  $\theta$ -mode falls in any unstable tongues solution will grow, resulting in instability. This condition is given as

$$\left(\frac{N}{\omega}\right)^2 > \mathcal{G}(f, F), \quad (3.1)$$

where  $\mathcal{G}(f, F)$  denotes the extreme left boundary of the first leftmost sub-harmonic tongue (see figure 1a). With time evolution,  $L$  grows due to unstable  $\theta$ -modes and the right end ( $(N/\omega)^2$ ) of the blue line (solid) segment (figure 1a) enters the first sub-harmonic tongue as indicated by the blue  $\times$  at  $(N/\omega)^2 = 0.4$  in figure 1b. At this instant, many frequencies ( $\in [(f/\omega)^2, (N/\omega)^2]$ ) are excited, corresponding to an angle  $\theta \in [0, \pi/2]$  and growth rates  $\sigma$ , as depicted by the inclined dashed blue segment in figure 1b. The sub-harmonic instabilities are triggered in this regime resulting in the intense growth of  $L$  (Singh & Pal

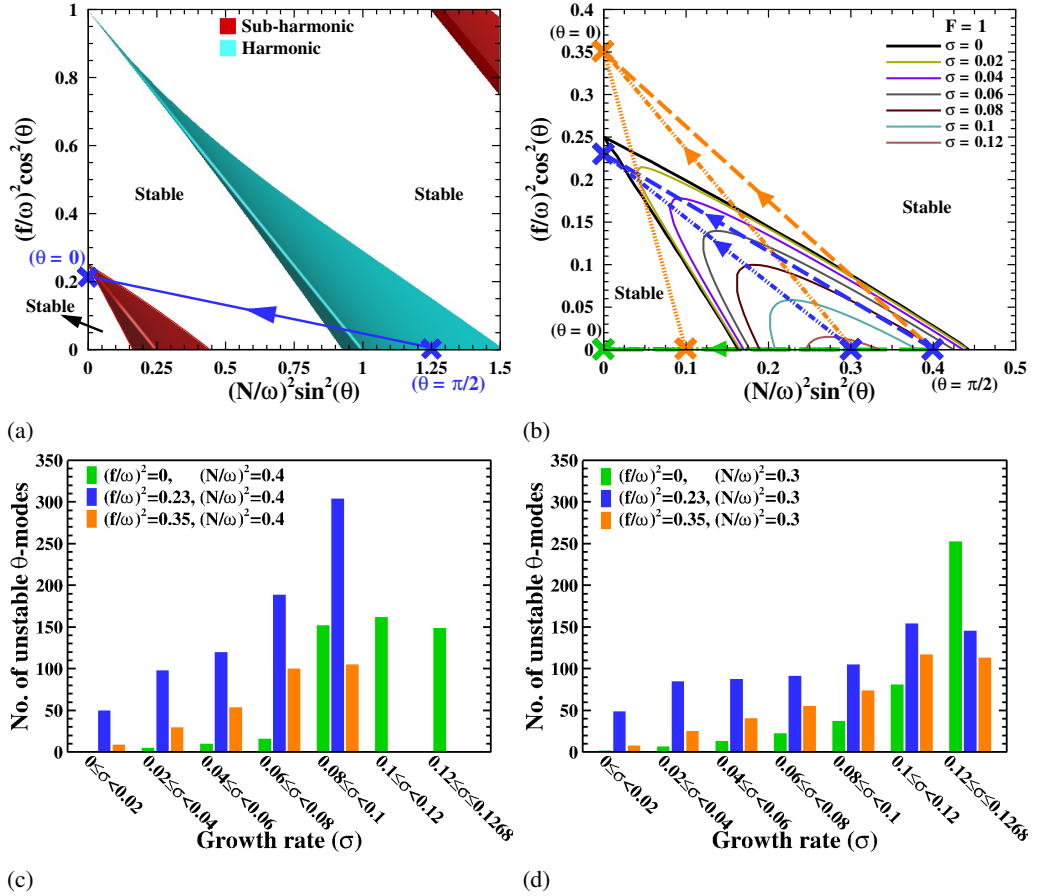


Figure 1: (a) Stability diagram for the solutions to the Mathieu equation 2.5 (Singh & Pal 2022) at forcing amplitude  $F = 1$ . The stable (white) regions are in between the unstable red (sub-harmonic) and cyan (harmonic) colored tongues. The inclined blue line (solid) segment represents the frequencies excited, corresponding to an angle  $\theta \in [0, \pi/2]$ , for a given  $(f/\omega)^2 = 0.23$  (left end ( $\times$ ) at  $\theta = 0$ ), and initial condition  $(N_0/\omega)^2$  (right end ( $\times$ ) at  $\theta = \pi/2$ ) in the first harmonic tongue. Arrow indicates the evolution of  $(N/\omega)^2$  as the mixing zone size- $L$  increases. Panel (b) is an enlargement of the first leftmost sub-harmonic tongue in (a). The black curve denotes the neutral stability curve for the growth rate  $\sigma = 0$ . The color curves respectively denote the contours of different growth rates ( $\sigma$ ) at intervals of 0.02. The dashed and dash-dotted green, blue and orange segments demonstrate the non-rotating case  $(f/\omega)^2 = 0$  and rotating cases  $(f/\omega)^2 = 0.23$  and 0.35, respectively, when  $(N/\omega)^2$  reaches to 0.4 and 0.3 during the growth of  $L$ . The possible number of unstable  $\theta$ -modes permitted to grow at various growth rates ( $\sigma$ ) for each  $(f/\omega)^2 = 0, 0.23$ , and 0.35 cases are shown in (c) when  $(N/\omega)^2 = 0.4$ , and (d) when  $(N/\omega)^2 = 0.3$ .

2022). The process repeats, and  $(N/\omega)^2$  moves to 0.3, as indicated by the dash-dotted blue segment. The instability finally saturates when  $(N/\omega)^2$  crosses the extreme left neutral stability curve (black) i.e.,  $(N/\omega)^2 = \mathcal{G}(f, F)$ . The instability condition 3.1 is no longer fulfilled, and  $L$  saturates. The horizontal green and inclined orange segments (both dash and dash-dotted) represent the cases without rotation  $(f/\omega)^2 = 0$  and with rotation  $(f/\omega)^2 = 0.35$ , respectively. We note here that the instability saturates for  $(f/\omega)^2 < 0.25$ .



An interesting feature for  $(f/\omega)^2 \geq 0.25$  is observed when  $(N/\omega)^2$  moves into the leftmost stable regime as indicated by the dotted orange segment (inclined). This segment must always pass through the first sub-harmonic tongue. The instability condition 3.1 is always satisfied, and  $L$  will continue to grow. Therefore, the instability will never saturate.

Figure 1c depicts the possible number of unstable  $\theta$ -modes permitted to grow at various growth rates  $\sigma$ , when  $(N/\omega)^2 = 0.4$  for each  $(f/\omega)^2 = 0, 0.23,$  and  $0.35$  cases. Here, the green, blue, and orange bars correspond to the dashed green, blue, and orange segments are shown in figure 1b. For a given  $(f/\omega)^2$  and  $(N/\omega)^2$ , we assume a step size of 0.1 between the  $\theta$  angles while calculating the number of  $\theta$ -modes between different growth rates with 0.02 size intervals, except for the last interval, which spans from 0.12 to 0.1268 and contains the maximum growth rate. In the non-rotating case  $(f/\omega)^2 = 0$ , the growth rate of the fastest growing  $\theta$ -modes is  $0.12 \leq \sigma \leq 0.1268$  (see figure 1c). However, the growth rate of the fastest growing modes in the rotating case  $(f/\omega)^2 = 0.23$  ( $0.08 \leq \sigma < 0.1$ ) is less compared to the non-rotating case. Therefore, the mixing zone size- $L$  will increase (or  $(N/\omega)^2$  decrease) gradually for  $(f/\omega)^2 = 0.23$ , than the rapid increase of  $L$  (or decrease of  $(N/\omega)^2$ ) for the non-rotating case. This results in a longer sub-harmonic instability phase for rotating case  $(f/\omega)^2 = 0.23$  as compared to the non-rotating case. The sub-harmonic instability phase is the time interval between the onset and the saturation of the sub-harmonic instability. At a higher rotation rate  $(f/\omega)^2 = 0.35$ , fewer fastest growing  $\theta$ -modes have a growth rate  $0.8 \leq \sigma < 0.1$  as compared to  $(f/\omega)^2 = 0.23$  (see a comparison among blue and orange bars in figure 1c). This demonstrates that  $L$  increases much more gradually for  $(f/\omega)^2 = 0.35$  than  $(f/\omega)^2 = 0.23$ . Figure 1d illustrates that at a later instant, when  $(N/\omega)^2 = 0.3$  and  $(f/\omega)^2 = 0$ , only a small number of  $\theta$ -modes are permitted to grow at smaller growth rates  $\sigma < 0.08$ , whereas a large number of unstable modes grows at larger growth rates  $\sigma \geq 0.08$ . The scenario is different for  $(f/\omega)^2 = 0.23$ , where a significant number of unstable modes are permitted to grow at all growth rates. This results in the triggering of more sub-harmonic instabilities and suggests an increase in turbulent kinetic energy (*t.k.e.*) for cases with  $0 < (f/\omega)^2 < 0.25$  as compared to the non-rotating case since sub-harmonic instabilities are responsible for the turbulent mixing (Singh & Pal 2022). Although, more unstable modes are permitted to grow at growth rates upto  $\sigma < 0.12$  for  $(f/\omega)^2 = 0.35$  compared to  $(f/\omega)^2 = 0$ , a significantly less number of fastest growing modes grow at  $0.12 \leq \sigma \leq 0.1268$ . This suggests that higher rotation rates,  $(f/\omega)^2 \geq 0.25$ , have weaker turbulence.

Figure 2a illustrates the stability diagram at forcing amplitude  $F = 3$ . The contour curves for the growth rates, from  $\sigma = 0$  to  $\sigma = 0.28$  with a step size of 0.04, in the first leftmost sub-harmonic tongue, are shown in figure 2b. We can observe that with an increase in  $F$ , the first sub-harmonic and harmonic tongues become wider, and the stable region between these tongues shrinks resulting in the early onset of the sub-harmonic instability and turbulent mixing similar to the non-rotating case (Singh & Pal 2022). Additionally, for all  $(f/\omega)^2$  cases, the maximum growth rate ( $\sigma_{max}$ ) of the fastest growing modes is 2.7 times greater at  $F = 3$  than at lower forcing amplitude ( $F = 1$ ) i.e.,  $\sigma_{max} = 0.338$  at  $F = 3$ , whereas  $\sigma_{max} = 0.1268$  at  $F = 1$ . As a result, the sub-harmonic instability is triggered earlier at  $F = 3$  than for  $F = 1$ . This suggests that the sub-harmonic instability phase at  $F = 3$  is shorter than the sub-harmonic instability phase at  $F = 1$  for  $(f/\omega)^2 < 0.25$  cases. Similar to the cases at  $F = 1$ , the instability saturates for  $(f/\omega)^2 < 0.25$ , whereas the instability never saturates for  $(f/\omega)^2 \geq 0.25$  and  $L$  continues to grow at  $F = 3$ , owing to the continuous triggering of the unstable  $\theta$ -modes as demonstrated by the dotted orange segment in figure 2b. These predictions from the linear stability analysis will further support our numerical



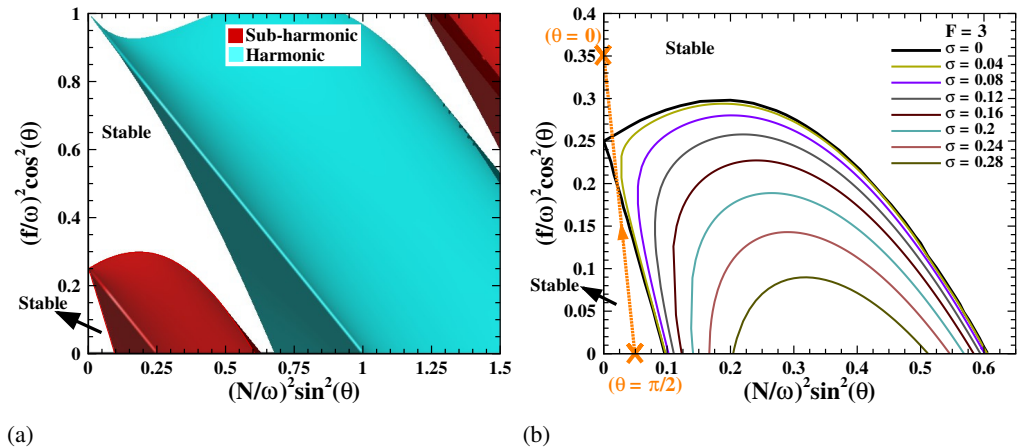


Figure 2: (a) Stability diagram for the solutions to the Mathieu equation 2.5 (Singh & Pal 2022) at  $F = 3$ . Panel (b) is the enlargement of the first leftmost unstable sub-harmonic (red) tongue of panel (a). The unstable sub-harmonic region is bounded by the black neutral stability curve for the growth rate  $\sigma = 0$  and the color curves represent the contours of different growth rates ( $\sigma$ ) at intervals of 0.04. The dotted orange segment demonstrate the rotating case  $(f/\omega)^2 = 0.35$ . The arrow indicates the evolution of  $(N/\omega)^2$  as the mixing zone size- $L$  increases.

simulations as presented in the next section.

### 3.2. Numerical simulations

The evolution of the vertically ( $x_3$ ) integrated turbulent kinetic energy ( $t.k.e.$ ) for  $F = 1$  is illustrated in figure 3a. The  $t.k.e.$  is defined as

$$t.k.e. = \frac{\langle u_1^2 \rangle_H + \langle u_2^2 \rangle_H + \langle u_3^2 \rangle_H}{2}, \quad \mathbf{u} = \mathbf{U} - \langle \mathbf{U} \rangle_H. \quad (3.2)$$

Here,  $\langle \mathbf{U} \rangle_H(x_3, t)$  is the horizontally averaged mean velocity field and  $\mathbf{u}(x_1, x_2, x_3, t)$  is the fluctuating velocity field. The  $t.k.e.$  rapidly grows for  $F1f/\omega 0$  and  $F1f/\omega 48$  during the onset of the sub-harmonic instability. Eventually, the  $t.k.e.$  decays owing to the instability saturation. The  $t.k.e.$  for  $F1f/\omega 48$  is higher than  $F1f/\omega 0$  due to the excitement of more unstable  $\theta$ -modes in the sub-harmonic region that are permitted to grow with growth rates ( $\sigma$ ) ranging from 0 to 0.1268, as observed from the stability analysis. The  $t.k.e.$  decreases significantly for  $f/\omega = 0.59$  (case  $F1f/\omega 59$ ) due to the effect of strong rotation. The excitement of a small number of unstable  $\theta$ -modes at higher growth rates, as predicted from the linear stability analysis, is also a possible reason for the low  $t.k.e.$  for  $F1f/\omega 59$ . Although small, the  $t.k.e.$  for  $F1f/\omega 59$  sustains owing to the continuous triggering of the sub-harmonic instability, resulting in continuous turbulent mixing. A similar evolution of  $t.k.e.$  is observed for  $F = 0.75$ . At a higher forcing amplitude of  $F = 3$ , turbulence appears at the beginning, and therefore,  $t.k.e.$  is similar for all  $f/\omega$  cases (figure 3b), indicating that the instability delaying effect of rotation is mitigated by the strong vertical forcing. Notice that the maximum value of  $t.k.e.$  for  $F1f/\omega 48$  is higher than  $F3f/\omega 48$ . This observation is also true for the non-rotating cases at the respective forcing amplitudes. The longer sub-harmonic instability phase for  $F1f/\omega 48$  is the reason for a higher value of  $t.k.e.$  at  $F1f/\omega 48$  than at  $F3f/\omega 48$ . The sub-harmonic instability phase is demonstrated using the shaded regions in the evolution of the mixing zone size  $L$  in the inset of figures 3a and 3b.

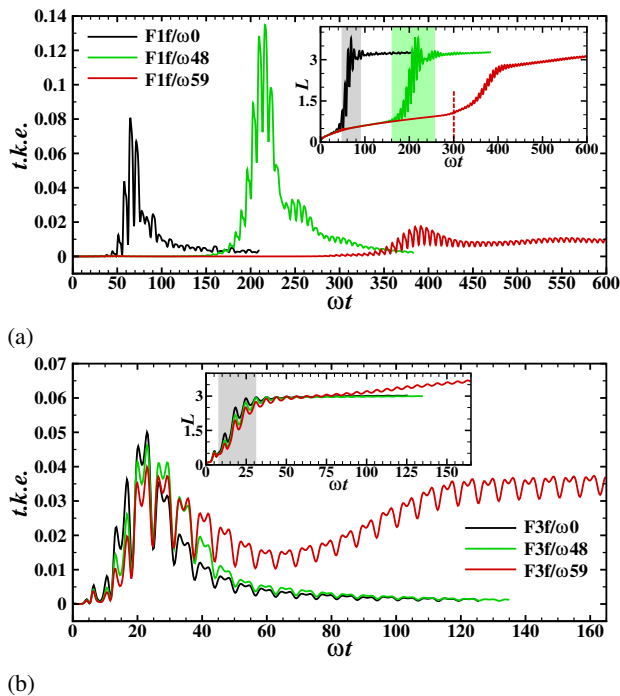


Figure 3: Evolution of vertically ( $x_3$ ) integrated  $t.k.e.$  for both without ( $f/\omega = 0$ ) and with ( $f/\omega = 0.48, 0.59$ ) rotation cases at (a)  $F = 1$ , and (b)  $F = 3$ . Inset shows the evolution of mixing zone size- $L$  with shaded regions indicating the sub-harmonic instability phase. The vertical red dashed line in the inset of panel (a) denotes the onset of sub-harmonic instability for  $F1f/\omega59$ .

A longer sub-harmonic instability phase for  $F = 0.75, 1$  signifies a delay in the saturation of the instabilities triggered during the low amplitude oscillations. Therefore, the instabilities get sufficient time to evolve, eventually resulting in turbulence. In contrast to  $F = 0.75, 1$ , at  $F = 2, 3$ , the sub-harmonic instability phase is short. The instabilities saturate quickly and therefore do not get sufficient time to evolve and intensify turbulence. This observation is consistent with our linear stability analysis that predicts the maximum growth rate of the fastest growing modes is 2.7 times greater at  $F = 3$  than  $F = 1$ , resulting in the shorter sub-harmonic instability phase at  $F = 3$ . Interestingly, both  $F2f/\omega59$  (figure not shown) and  $F3f/\omega59$  manifest a recovery in  $t.k.e.$  owing to the continuous triggering of the sub-harmonic instabilities.

The transition to turbulence phenomenon for the cases without and with rotation is analyzed using the contour plots of the concentration fields in a vertical plane. Figure 4 depicts the evolution of the interface of the concentration field for  $F1f/\omega0$ . The initially perturbed interface, subjected to vertical and periodic accelerations, deforms into a wavy form owing to harmonic and sub-harmonic resonance as shown in figure 4a at  $\omega t = 33.6$ . This diffused wavy interface is amplified by the sub-harmonic instability, leading to the formation of mushroom-shaped waves as shown in figure 4b at  $\omega t = 49$ . At this instance, some waves with shorter wavelengths become disorganized and interact with each other, resulting in small velocity fluctuations. In the next oscillation, the amplitude of a longer wavelength wave amplifies, leading to the birth of a well-defined mushroom-shaped wave that bursts at the nodes as depicted in figure 4c at  $\omega t = 56$ . This process is known as

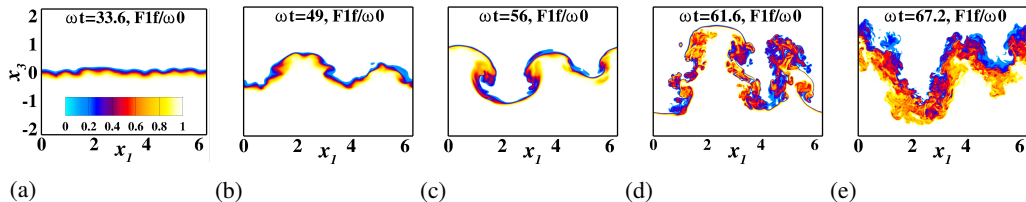


Figure 4: Contours of concentration field in vertical  $x_1 - x_3$  center plane ( $x_2 = \pi$ ) for case  $F1f/\omega 0$  at time instants (a)  $\omega t = 33.6$ , (b)  $\omega t = 49$ , (c)  $\omega t = 56$ , (d)  $\omega t = 61.6$ , and (e)  $\omega t = 67.2$ . Pure fluids of  $C = 1$  (denser) and  $C = 0$  (lighter) are made transparent.

wave-breaking of the Faraday waves (Cavelier *et al.* 2022) and is responsible for the onset of irreversible mixing. In the successive oscillations, the entire interface breaks down into small-scale structures leading to a full transition to turbulence as manifested in figures 4d and 4e. A similar dynamics is observed for  $F = 0.75$  and  $f/\omega = 0$  (see Movie 1 and Movie 4).

The combined effect of vertical oscillation and rotation in  $F1f/\omega 48$  results in roll-ups at multiple locations on the diffuse interface as shown in figure 5a at  $\omega t = 175.28$ . In subsequent oscillations, roll-ups will continue to form with a large size but in the opposite direction to that of the previous one. These roll-ups will finally break into turbulence (see figure 5a). Notice that the entire interface layer breaks into small structures in one oscillation resulting in a larger thickness of the turbulent mixing region as compared to  $F1f/\omega 0$  where the mushroom-shaped wave first breaks at the nodes and then turbulence spreads to the entire interface layer in the subsequent oscillations. Movie 2 included as the supplementary data demonstrates this event. The formation of the roll-ups and their eventual breaking to turbulence is responsible for larger *t.k.e.* in  $F1f/\omega 48$  as compared to  $F1f/\omega 0$  (figure 3a). This phenomenon is consistent with our linear stability analysis as follows. For  $F1f/\omega 48$  a significant number of unstable modes are permitted to grow at all growth rates. This has been demonstrated in figures 1c and 1d when  $(N/\omega)^2 = 0.4$  and  $0.3$  respectively. The  $\omega t$  corresponding to  $(N/\omega)^2 = 0.4$  and  $0.3$  is in the range  $175 - 205$ . Figure 5a shows the formation of the roll-ups at  $\omega t = 193.2$ , and therefore it can be deduced that the unstable modes promote the formation of roll-ups that break to enhance *t.k.e.* for  $F1f/\omega 48$ . We observe similar dynamics for  $F075f/\omega 48$  (see Movie 5). This phenomenon results in a gradual increase of irreversible mixing. When the Coriolis frequency increase to  $f/\omega = 0.59$  (case  $F1f/\omega 59$ ), we found that the effect of rotation is strong enough to suppress the formation of large amplitude waves and roll-ups. Therefore, the turbulent mixing is only caused by the finger-shaped instability as depicted in figure 5b (see supplementary Movie 3 and Movie 6).

At higher forcing amplitude  $F = 3$  for  $f/\omega = 0.48$ , we observe the development of random finger-shaped structures on the interface that break in the first oscillation as shown in the figure 5c. Therefore, the turbulent mixing starts from the beginning of the periodic forcing. Additionally, the intensity of turbulence is low because of the shorter sub-harmonic instability phase at higher  $F$ . As the instability delaying effect of rotation is subdued at higher forcing amplitudes (Singh & Pal 2022), the turbulent mixing occurs by this mechanism for all  $f/\omega$  at  $F = 2, 3$  (figures not shown). We have included the animation of the concentration field for  $F3f/\omega 48$  as supplementary data (Movie 7).

Since there is no mean velocity field involved, we start the analysis of the irreversible

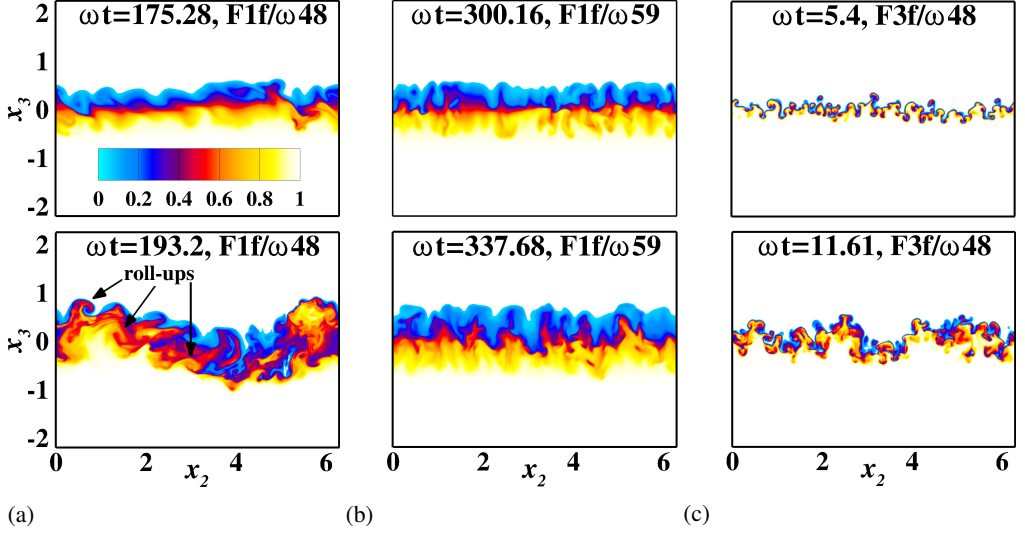


Figure 5: Contours of concentration field in vertical  $x_2 - x_3$  center plane ( $x_1 = \pi$ ) for rotation cases (a)  $F1f/\omega 48$ , (b)  $F1f/\omega 59$ , and (c)  $F3f/\omega 48$  at different time instants during the instability growth stage.

mixing using the *t.k.e.* evolution equation as follows:

$$\frac{dt.k.e.}{dt} = \mathcal{P} - S - B - \epsilon - \frac{\partial \mathcal{T}_j}{\partial x_j}. \quad (3.3)$$

The turbulent production term  $\mathcal{P} = -\langle u_i u_j \rangle_H \frac{\partial \langle U_i \rangle_H}{\partial x_j}$  and the transport term  $\partial \mathcal{T}_j / \partial x_j$ , where  $\mathcal{T}_j = \langle p u_j \rangle_H - 2\nu \langle s_{ij} u_i \rangle_H + \frac{1}{2} \langle u_i u_i u_j \rangle_H$  are negligible. The energy input from the periodic forcing is  $S = 2\mathcal{A}g_0 F \cos(\omega t) \langle u_3 c \rangle_H$ . The buoyancy flux  $B = 2\mathcal{A}g_0 \langle u_3 c \rangle_H$  accounts for the reversible rate of exchange between *t.k.e.* and the potential energy. The viscous dissipation  $\epsilon = 2\nu \langle s_{ij} s_{ij} \rangle_H$ , where  $s_{ij} = (\partial u_i / \partial x_j + \partial u_j / \partial x_i) / 2$ , acts as a sink for *t.k.e.*. We obtain an excellent closure of equation 3.3 for all the simulations signifying sufficient grid spacing in all directions to resolve all length scales.

The irreversible mixing is characterized by partitioning the total potential energy (PE)  $E_p = 2\mathcal{A}g_0 \int_V C(\mathbf{x}) x_3 dV$  into the sum of an available potential energy (APE)  $E_a$  and background potential energy (BPE)  $E_b$  (Winters *et al.* 1995). The BPE is the minimum potential energy a flow can have and is unavailable for extraction from the potential energy reservoir for driving macroscopic fluid motion. To estimate BPE of the flow at any instance of time, a volume element  $dV$  with concentration  $C$  at height  $x_3$  is adiabatically relocated to  $x_3^*$  such that the redistributed concentration field is statistically stable ( $dC(x_3^*)/dx_3^* \leq 0$ ) everywhere. We compute  $E_b = 2\mathcal{A}g_0 \int_V C(x_3^*) x_3^* dV$  and subtract it from  $E_p$  to obtain  $E_a$  (Winters & Barkan 2013; Chalamalla & Sarkar 2015).  $E_a$  is available to be converted into kinetic energy. Since our domain is closed by the top and bottom boundaries, the surface fluxes are zero. We derive the simplified equations for the evolution of PE, BPE, and APE following Winters *et al.* (1995),

$$\frac{dE_p}{dt} = B_V + \phi_i, \quad (3.4a)$$

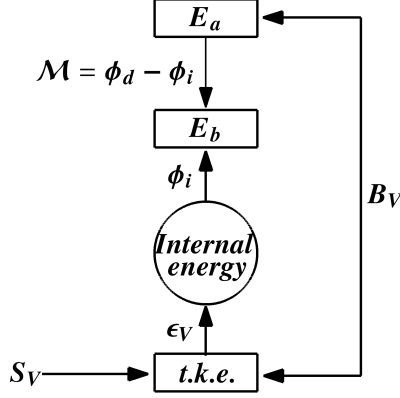


Figure 6: Schematic of energy pathways:  $S_V$  is the volume integrated  $S$  denoting the external input of energy from periodic forcing,  $B_V$  is reversible buoyancy flux,  $M$  is irreversible mixing rate due to purely turbulent mixing,  $\phi_d$  is irreversible diapycnal flux,  $\phi_i$  is conversion of internal to potential energy due to laminar diffusion, and  $\epsilon_V$  is kinetic energy dissipation.

$$\frac{dE_b}{dt} = \phi_d, \quad (3.4b)$$

$$\frac{dE_a}{dt} = B_V - (\phi_d - \phi_i). \quad (3.4c)$$

Here  $B_V$ ,  $\phi_i$ , and  $\phi_d$  are integrated over the volume  $V = l_{x_1} l_{x_2} (2H - 2H_s)$ , and  $(2H - 2H_s)$  is the vertical height of the domain excluding top and bottom sponge layer thickness. The  $B_V = \int B l_{x_1} l_{x_2} dx_3$  is volume integrated buoyancy flux and  $\phi_i = -2\mathcal{A}g_0\kappa A (\langle C_{top} \rangle_H - \langle C_{bot} \rangle_H)$ , where  $A = l_{x_1} l_{x_2}$ , the rate at which the potential energy of a statically stable concentration ( $C$ ) distribution increases in the absence of macroscopic fluid motion through the irreversible conversion of internal to potential energy. The  $\phi_i$  is a strictly non-negative quantity and signifies the increase in BPE at a constant rate  $\phi_i$  owing to the laminar diffusion.  $\phi_d = 2\mathcal{A}g_0\kappa \int_V -\frac{dx_3^*}{dC} |\nabla C|^2 dV$  represents the rate of change of BPE due to irreversible diapycnal flux and is a measure of the irreversible mixing. Notice that as  $\phi_d \geq 0$ ,  $E_b$  always increases as a result of diapycnal mixing.  $\phi_d$  is associated with the increase in BPE due to laminar diffusion and energy coming directly from the *t.k.e.* reservoir via  $B_V$  which is related to the turbulent mixing. We wish to investigate the energetics associated with the turbulent mixing caused by the sub-harmonic instability. Therefore, we define the irreversible mixing rate  $\mathcal{M} (= \phi_d - \phi_i)$  to isolate the increase in BPE due to purely turbulent mixing from that of laminar diffusion (Peltier & Caulfield 2003). Since we have periodic forcing in the domain, we choose to calculate the cumulative mixing efficiency (Peltier & Caulfield 2003; Briard *et al.* 2019) as follows:

$$\eta_{cu}(t) = \frac{\int_0^t \mathcal{M} dt}{\int_0^t (\mathcal{M} + \epsilon_V) dt}. \quad (3.5)$$

Here  $\epsilon_V = \int \epsilon l_{x_1} l_{x_2} dx_3$  is the volume integrated viscous dissipation. The cumulative mixing efficiency  $\eta_{cu}$  measures the irreversible loss of *t.k.e.* that expends in irreversible turbulent mixing in contrast to the total *t.k.e.* loss to the irreversible turbulent mixing and viscous dissipation.

Figure 6 illustrates the energy pathways. Arrows denote the energy exchanges between

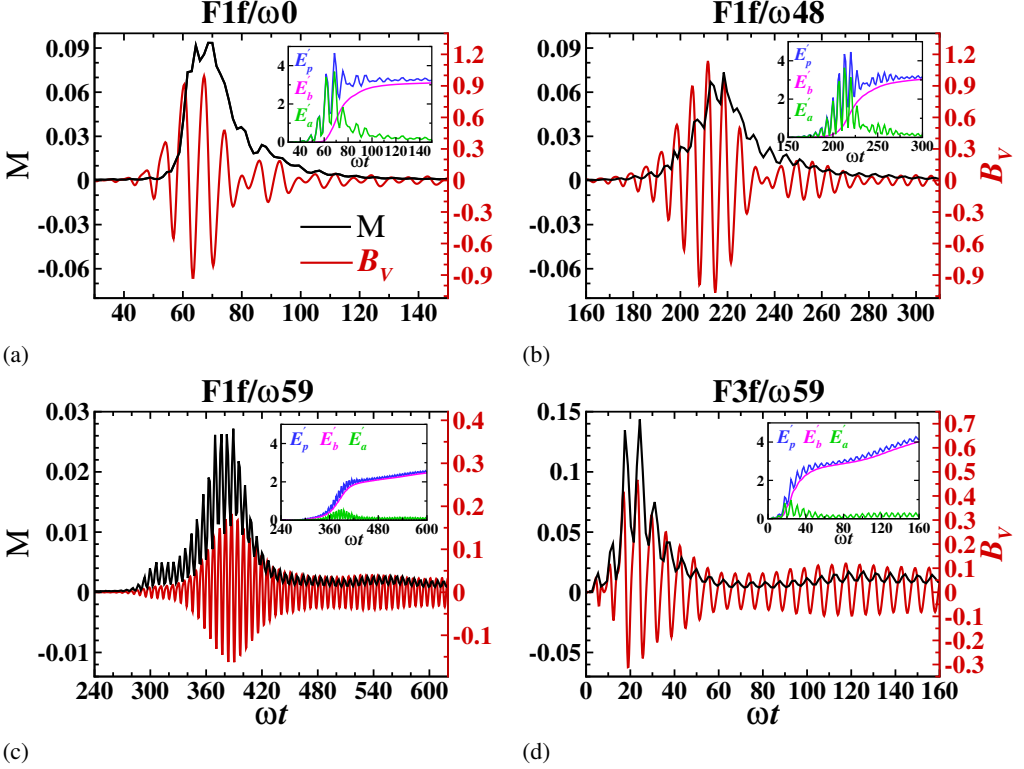


Figure 7: Time evolution of buoyancy flux ( $B_V$ ) and irreversible mixing rate ( $M$ ) at  $F = 1$  for (a)  $f/\omega = 0$ , (b)  $f/\omega = 0.48$ , (c)  $f/\omega = 0.59$ , and at  $F = 3$  for (d)  $f/\omega = 0.59$ . The corresponding time evolution of change in PE ( $E_p'(t) = E_p(t) - E_p(0) - \phi_i t$ ), BPE ( $E_b'(t) = E_b(t) - E_b(0) - \phi_i t$ ), and APE ( $E_a'(t) = E_p'(t) - E_b'(t)$ ), due to irreversible turbulent mixing are shown in the inset of each panel.

different energy reservoirs.  $S_V$  depicts the input rate of external energy to the *t.k.e.* reservoir. In the presence of fluid motion due to turbulent mixing, *t.k.e.* enters the potential energy reservoir via reversible buoyancy flux  $B_V$ , increasing  $E_a$ . Some part of  $E_a$  can go to  $E_b$  via purely turbulent mixing as quantified by  $M$ , resulting in irreversible mixing. The remaining portion of  $E_a$  converts back to *t.k.e.* by  $B_V$ . The energy loss from the *t.k.e.* reservoir to the internal energy reservoir occurs through viscous dissipation  $\epsilon_V$ . The laminar diffusion contributes energy to  $E_b$  directly via  $\phi_i$ .

Figure 7 illustrates the temporal evolution of the reversible buoyancy flux  $B_V$  and the irreversible mixing rate  $M$ . We also include the evolution of  $E_p'$ ,  $E_b'$ , and  $E_a'$  in the inset of each figure.  $E_p'$  and  $E_b'$  demonstrate the total change in PE and BPE due to irreversible turbulent mixing and are calculated relative to their initial values.  $E_a'$  ( $=E_p' - E_b'$ ) denotes the corresponding change in APE. The cumulative energy changes in PE and BPE associated with the constant rate of laminar diffusion are not included in  $E_p'$  and  $E_b'$ . Therefore,  $E_p(t)' = E_p(t) - E_p(0) - \phi_i t$  and  $E_b(t)' = E_b(t) - E_b(0) - \phi_i t$ , where  $t$  is the time from the start of the simulation. The *t.k.e.* for  $F1f/\omega 0$  increases due to the onset of sub-harmonic instabilities and the formation and breaking of mushroom-shaped waves. This increased *t.k.e.* results in an increase in  $B_V$  at  $\omega t \simeq 46 - 55$ , and therefore, the potential energy of the flow also increases as demonstrated in figure 7a. The PE is stored as APE, which almost



returns to *t.k.e.* via  $B_V$  because the transfer of APE to BPE remains zero as quantified by  $\mathcal{M} \approx 0$ . In the subsequent oscillation, this *t.k.e.* contributes to the external energy input, resulting in the increased *t.k.e.* and wave-breaking. The  $\mathcal{M}$  also starts increasing after  $\omega t \approx 55$ . After wave-breaking, the entire interface layer breaks, resulting in a rapid increase of  $\mathcal{M}$  signifying rapid conversion of APE into BPE, and the APE decreases. When the instabilities saturate at  $\omega t \approx 70$ , *t.k.e.*, and  $B_V$  decrease, leading to a decrease in APE and PE saturates. The BPE also saturates, as demonstrated by a decreasing  $\mathcal{M}$ . Similar to  $F1f/\omega 0$ , we observe that  $B_V$  for  $F1f/\omega 48$  increases at  $\omega t \approx 180$  owing to an increase in *t.k.e.* (see figure 7b). At the same instance,  $B_V$ , PE, and APE also increase. We find a gradual increase of  $\mathcal{M}$  and BPE for  $F1f/\omega 48$  compared to a rapid increase for  $F1f/\omega 0$ . The reason is the continuous formation and breaking of the roll-ups at the diffuse interface during the sub-harmonic instability phase for  $F1f/\omega 48$ . With the saturation of the instability,  $B_V$  and APE start decreasing, resulting in the increase and eventual saturation of BPE as illustrated by the gradual decrease of  $\mathcal{M}$  to zero in figure 7b. This gradual decrease in  $\mathcal{M}$  denotes that irreversible mixing is sustained for an extended period than  $F1f/\omega 0$ , owing to the long sub-harmonic instability phase. For  $F1f/\omega 59$ , there is a significant delay in the onset of sub-harmonic instability due to the presence of the stable region where no harmonic or sub-harmonic modes are excited (Singh & Pal 2022). This stable region is apparent in the evolution of mixing zone size- $L$  for  $F1f/\omega 59$  as shown in the inset of figure 3a. Therefore,  $B_V$  and APE  $\sim 0$  till  $\omega t \approx 280$ . During this period, the initial concentration profile diffuses while maintaining its static stability (Winters *et al.* 1995). The flow remains in its reference state of minimum potential energy till the onset of turbulent mixing, signifying  $E_p = E_b$  from the definition of  $E_b$ . No APE is created and  $\phi_d = \phi_i$  (from equations 3.4a, 3.4b and 3.4c) signifying the increase in BPE via  $\phi_i$ . Therefore, the potential energy increases at the expense of the internal energy of the fluid. We find,  $\phi_d(0.001) \approx \phi_i(0.0008)$  till  $\omega t \approx 280$ . A similar phenomenon is also observed for  $F1f/\omega 48$ , and for all  $f/\omega$  at  $F = 0.75$ . For higher rotation rate the turbulence is weaker (see Movie 3), resulting in smaller *t.k.e.* and  $B_V$  (figure 7c) compared to the previous cases.  $B_V$  increases after  $\omega t \approx 280$ , increasing APE. The major portion of the APE coming from *t.k.e.* via  $B_V$  is transferred to BPE via  $\mathcal{M}$ . As a result, only a minor portion of the APE is available for reversible exchange back to *t.k.e.*, as shown by small APE in the inset of figure 7c. Therefore, in the subsequent oscillation, only a small amount of kinetic energy is available in the *t.k.e.* reservoir, which contributes to the external energy input, resulting in weaker turbulence. The instability never saturates for  $F1f/\omega 59$  and triggers continuously, resulting in the sustenance of *t.k.e.* and  $B_V$ . The PE also continues to increase due to  $B_V$ , and APE continues to remain small since much of the APE goes to BPE.  $\mathcal{M}$  oscillates and remains greater than zero indicating a continuous increase in BPE with time and signifying the sustenance of irreversible mixing for higher rotation rates.

For higher forcing amplitudes  $F = 2, 3$  and  $f/\omega = 0, 0.48$ , the *t.k.e.* and  $B_V$  increase from the beginning of the periodic forcing, resulting in the increase of APE (figure not shown). Subsequently, BPE and  $\mathcal{M}$  also increase. Since the instabilities saturate quickly for these cases,  $B_V$  and APE become approximately zero. The BPE saturates, and the  $\mathcal{M}$  also tends to zero, signifying the ceasing of irreversible mixing. The initial evolution of energetics for  $F = 2, 3$  for  $f/\omega = 0.59$  (figure 7d for  $F3f/\omega 59$ ) is similar to the cases discussed above. However, at a later stage, the evolution resembles the case  $F1f/\omega 59$  and demonstrates non-zero  $B_V$  and  $\mathcal{M}$ , signifying a continuous increase in BPE and sustenance of irreversible turbulent mixing.

The time evolution of the cumulative mixing efficiency  $\eta_{cu}$  is plotted in figure 8. We report the  $\eta_{cu}$  values when the instability saturates for  $f/\omega = 0$  and  $0.48$  cases. Since the instability



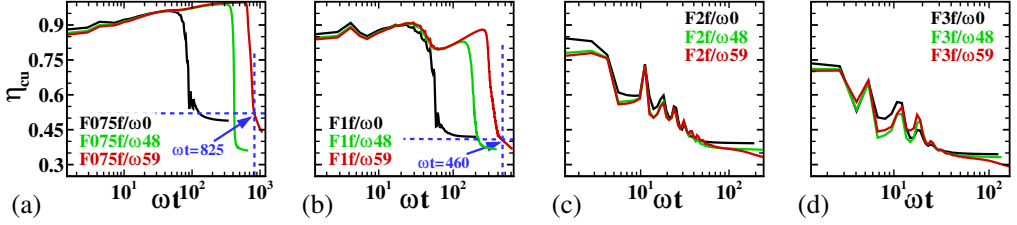


Figure 8: Time evolution of cumulative mixing efficiency  $\eta_{cu}$  for each without rotation ( $f/\omega = 0$ ) and with rotation ( $f/\omega = 0.48, 0.59$ ) cases at forcing amplitudes (a)  $F = 0.75$ , (b)  $F = 1$ , (c)  $F = 2$ , and (d)  $F = 3$ .

never saturates for  $f/\omega = 0.59$ , the  $\eta_{cu}$  is given when  $\mathcal{M}$  decreases to its approximately minimum value after reaching its peak. For  $F075f/\omega0$  case,  $\eta_{cu}$  decreases rapidly when the irreversible mixing rate  $\mathcal{M}$  and the viscous dissipation  $\epsilon_V$  increases. It attains a minimum value of  $\sim 0.495$  after instability saturation. In the presence of rotation for  $F075f/\omega48$ , the  $\eta_{cu}$  reduces to  $\sim 0.363$ , which implies that the mixing is not as efficient as for  $F075f/\omega0$ . For  $F075f/\omega59$ , the  $\eta_{cu}$  decreases continuously owing to the continuous irreversible mixing. However, the mixing is still more efficient ( $\eta_{cu} \approx 0.52$  at  $\omega t \approx 825$ ) than  $F075f/\omega0$  and  $F075f/\omega48$ . For  $F1f/\omega0$ ,  $\eta_{cu}$  is  $\sim 0.421$  similar to that obtained by Briard *et al.* (2019). At  $F = 1$  and  $f/\omega = 0.48$   $\eta_{cu} \sim 0.372$  whereas for  $f/\omega = 0.59$  the cumulative mixing efficiency is  $0.406$  at  $\omega t = 460$ , but keeps decreasing with time. We find that the mixing becomes less efficient with an increase in  $F$  for all  $f/\omega$  values, and the mixing efficiency continues to decrease for the  $f/\omega = 0.59$  cases. In the present work, the primary mechanism for mixing vertically oscillating stably stratified fluids is the Faraday instability. In density-stratified shear flows the Kelvin-Helmholtz instability is responsible for mixing. Despite this difference in the mixing mechanisms, the cumulative mixing efficiencies obtained in our simulations are surprisingly similar to those of the stratified shear turbulent flows (Gregg *et al.* 2018).

#### 4. Conclusions

We perform DNS to investigate the effect of rotation on the turbulent mixing driven by the Faraday instability in two miscible fluids subjected to vertical oscillations. At lower forcing amplitudes  $F = 0.75$  and  $1$ , the *t.k.e.* increases with an increase in the Coriolis frequency from  $f/\omega = 0$  to  $0.48$ . This enhancement is attributed to the excitement of more unstable  $\theta$ -modes in the sub-harmonic region that results in the development and breaking of roll-ups at the interface layer during the sub-harmonic instability phase. The mechanism of turbulence generation for the cases without rotation is different. A well-defined mushroom-shaped wave evolves for  $f/\omega = 0$  cases that disintegrate at the nodes. Subsequently, the turbulence spreads to the entire mixing layer in successive oscillations. In contrast to  $f/\omega = 0, 0.48, f/\omega = 0.59$  have a weaker turbulence owing to the development and gradual breaking of finger-shaped structures. At higher forcing amplitudes  $F = 2$  and  $3$  for  $f/\omega = 0, 0.48$ , and  $0.59$ , we observe the breakdown of finger-shaped structures in the first two oscillations of periodic forcing resulting in the early onset of turbulence. However, the turbulence is less intense and short-lived than at lower forcing amplitudes owing to the shorter sub-harmonic instability phase. This shorter sub-harmonic instability phase at higher  $F$  is attributed to the higher growth rate of the fastest growing modes, which is  $2.7$  times larger for  $F = 3$  than  $F = 1$ , as determined by linear stability analysis. An interesting finding is an increase in *t.k.e.* after an initial decrease for  $f/\omega = 0.59$  due to the continuous triggering of the

sub-harmonic instabilities.

We also analyze the energetics associated with the flow. An increase in *t.k.e.* for the cases with  $f/\omega = 0.48$  at  $F = 0.75, 1$  implies an increase in the buoyancy flux  $B_V$  and therefore, APE also increases. Some part of this APE converts to BPE via irreversible mixing rate  $\mathcal{M}$  related to the turbulent mixing, whereas the rest is converted back to *t.k.e.* via  $B_V$ . When the *t.k.e.* starts decreasing due to instability saturation,  $B_V$  also decreases, signifying a decrease in APE. Therefore, BPE saturates, and  $\mathcal{M}$  approaches zero. Interestingly, for  $f/\omega = 0.48$  the irreversible mixing sustains for a longer period than  $f/\omega = 0$  due to a longer sub-harmonic instability phase. The cases with a higher rotation rate of  $f/\omega = 0.59$  demonstrate a significant delay in the onset of sub-harmonic instability, owing to which  $B_V$  and APE remain zero. The initial concentration profile diffuses during this period to increase total PE at the rate  $\phi_i$ . This PE goes completely to BPE at the same rate since  $\phi_d$  becomes equal to  $\phi_i$  according to equation 3.4c. After the onset of the sub-harmonic instability, the *t.k.e.*,  $B_V$ , and APE increase. However, these values remain significantly smaller than  $f/\omega = 0, 0.48$  cases. In contrast to cases  $f/\omega = 0, 0.48$ , for  $f/\omega = 0.59$  the bulk of the portion of APE expends to BPE via  $\mathcal{M}$  resulting in a transfer of a small amount of APE back to *t.k.e.* reservoir. Therefore, in the subsequent oscillation, only a small *t.k.e.* is available to contribute to the external energy input from periodic forcing, signifying weaker turbulence compared to  $f/\omega = 0, 0.48$  cases. Since the instabilities never saturate for  $f/\omega = 0.59$ , the *t.k.e.*,  $B_V$ , and APE although small remain non-zero. The  $\mathcal{M}$  remains greater than zero, signifying a continuous increase in BPE and irreversible turbulent mixing. At  $F = 2, 3$ ,  $\mathcal{M}$  increases from the beginning of the vertical forcing for all  $f/\omega$  cases. However, the irreversible mixing for  $f/\omega = 0, 0.48$  does not sustain for long owing to the quick saturation of the sub-harmonic instability. Since the instability never saturates for  $f/\omega = 0.59$ ,  $\mathcal{M}$  demonstrates continuous oscillations and therefore, continuous irreversible mixing. Finally, the mixing phenomenon is quantified using cumulative mixing efficiency. We conclude that for rotation rates  $(f/\omega)^2 > 0.25$  and at lower forcing amplitudes  $F = 0.75, 1$  the mixing process is more efficient because the major portion of APE expends to BPE via  $\mathcal{M}$ , compared to  $(f/\omega)^2 < 0.25$ .

**Supplementary data.** Supplementary movies are available at [https://doi.org/\\*\\*.\\*\\*\\*\\*/jfm.\\*\\*\\*...](https://doi.org/**.****/jfm.***...)

**Acknowledgements.** We gratefully acknowledge Dr. Vamsi K. Challamalla for providing us the computer program for the calculation of total PE,  $x_3^*$ , BPE and  $\phi_d$ . We also want to thank the Office of Research and Development, Indian Institute of Technology Kanpur for the financial support through grant no. IITK/ME/2019194. The support and the resources provided by PARAM Sanganak under the National Supercomputing Mission, Government of India at the Indian Institute of Technology, Kanpur are gratefully acknowledged.

**Declaration of interests.** The authors report no conflict of interest.

**Author contributions.** The authors contributed equally to analysing data and reaching conclusions, and in writing the paper.

## Appendix A. Floquet Analysis

The theorems related to the Floquet theory and the steps to solve the Mathieu equation (2.5) by using these theorems are briefly discussed here. Proofs of the theorems and solution steps can be found in Jordan & Smith (2007, pp. 308-317).

**THEOREM 1 (FLOQUET'S THEOREM).** Let  $\frac{d\vec{x}}{dt} = A(t)\vec{x}$ , be a first order linear differential system, where  $A(t)$  is  $T$ -periodic matrix such that  $A(t+T) = A(t), \forall t$ . This system has at

least one non-trivial solution  $\vec{x} = \vec{\chi}(t)$  such that

$$\vec{\chi}(t+T) = \mu \vec{\chi}(t), \quad \forall t \quad (\text{A } 1)$$

where  $\mu$  is a **characteristic number** or **Floquet multiplier**.

If  $\Phi(t)$  is a fundamental solution matrix of system  $\vec{x} = A(t)\vec{x}$ , then  $\Phi(t+T)$  is also a fundamental matrix, and there exists a non-singular matrix  $C$  such that,

$$\Phi(t+T) = C\Phi(t), \quad \forall t \quad (\text{A } 2a)$$

$$C = \Phi^{-1}(t)\Phi(t+T). \quad (\text{A } 2b)$$

Here, **characteristic numbers**,  $\mu$ 's, are the eigenvalues of  $C$ . We can obtain the matrix  $C = \Phi(T)$  for initial conditions at  $t = 0$  such that  $\Phi(0) = \mathbf{I}$ , where  $\mathbf{I}$  is the identity matrix.

**THEOREM 2.** For system  $\vec{x} = A(t)\vec{x}$ , where  $A(t)$  is  $T$ -periodic, with **characteristic numbers**  $\mu_1, \mu_2, \dots, \mu_n$ , the product of the **characteristic numbers** is obtained as:

$$\mu_1 \mu_2 \dots \mu_n = \exp \left( \int_0^T \text{tr}\{A(t)\} dt \right). \quad (\text{A } 3)$$

The **characteristic exponent** ( $\sigma$ ) of the system characterizing the growth rate of the instability is defined as  $e^{\sigma T} = \mu$ .

**THEOREM 3.** Let  $C$  has  $n$  distinct eigenvalues,  $\mu_i$  and corresponding  $\sigma_i, i=1,2,\dots,n$ . Then system  $\vec{x} = A(t)\vec{x}$  has  $n$  linearly independent solutions of the form:

$$\vec{\chi}_i(t) = e^{\sigma_i t} \vec{P}_i(t) \quad (\text{A } 4)$$

where  $\vec{P}_i(t)$  are the periodic vector functions with period  $T$ .

Clearly, **characteristic exponents**  $e^{\sigma_i t}$ , will determine the behaviour of the solutions (A 4). Now, we apply above theorems to the mathieu equation (2.5). The equation (2.5) can be rewrite as:

$$\ddot{a} + (\gamma + \alpha + \beta \cos \tau) a = 0, \quad (\text{A } 5)$$

where,

$$\gamma = \frac{f^2 \cos^2(\theta)}{\omega^2}; \quad \alpha = \frac{N^2 \sin^2(\theta)}{\omega^2}; \quad \beta = F \frac{N^2 \sin^2(\theta)}{\omega^2}. \quad (\text{A } 6)$$

We define  $a = X$  and  $\dot{a} = Y$  to express equation (A 5) as a first-order system, given as

$$\begin{bmatrix} \dot{X} \\ \dot{Y} \end{bmatrix} = \begin{bmatrix} 0 & 1 \\ -(\gamma + \alpha + \beta \cos \tau) & 0 \end{bmatrix} \begin{bmatrix} X \\ Y \end{bmatrix}. \quad (\text{A } 7)$$

In the notation of Theorem 1,

$$A(\tau) = \begin{bmatrix} 0 & 1 \\ -(\gamma + \alpha + \beta \cos \tau) & 0 \end{bmatrix}. \quad (\text{A } 8)$$

Here,  $A(\tau)$  is periodic with period  $2\pi$ . As  $\text{tr}\{A(\tau)\} = 0$ , the product of the **Characteristic numbers** of  $A(\tau)$  is  $\mu_1 \mu_2 = e^0 = 1$ . For the following initial condition

$$\Phi(0) = \begin{bmatrix} 1 & 0 \\ 0 & 1 \end{bmatrix}, \quad (\text{A } 9)$$

we obtain the matrix  $C = \Phi(T)$  by numerically integrating (with MATLAB<sup>®</sup>) the system (A 7) from  $\tau = 0$  to  $\tau = 2\pi$ .  $\mu_1$  and  $\mu_2$  are the solutions of characteristic equation of  $C$

$$\mu^2 - (\text{sum of roots})\mu + (\text{product of roots}) = 0, \quad (\text{A } 10)$$

and using  $\mu_1\mu_2 = 1$ , we get

$$\mu^2 - \phi(\gamma, \alpha, \beta)\mu + 1 = 0. \quad (\text{A } 11)$$

Here,  $\phi(\gamma, \alpha, \beta)$  represents the sum of roots. The solutions  $\mu_1$  and  $\mu_2$  of the equation (A 11) are

$$\mu_1, \mu_2 = \frac{1}{2} \left( \phi \pm \sqrt{(\phi^2 - 4)} \right). \quad (\text{A } 12)$$

Therefore, different values of  $\phi$  and corresponding  $\mu_1, \mu_2$  ( $\sigma_1$  and  $\sigma_2$  will determine the behaviour of solutions. When  $\phi > 2$ :  $\mu_1, \mu_2$  are both real and positive with  $\mu_1\mu_2 = 1$ , one of them, say  $\mu_1 > 1$  and  $\mu_2 < 1$ . The corresponding **characteristic exponents** are real and have the form  $\sigma_1 = \xi > 0$ ,  $\sigma_2 = -\xi < 0$  (because  $\sigma_2 = \ln(\mu_2)/T < 0$ ). So, the general solution from Theorem 3 can be written as:

$$X(\tau) = c_1 e^{\xi\tau} P_1(\tau) + c_2 e^{-\xi\tau} P_2(\tau), \quad (\text{A } 13)$$

where  $\xi > 0$ , thus  $e^{\xi\tau}$  corresponds to the exponential growth in time and solution becomes **unstable** with **harmonic** in nature. When  $\phi < -2$ :  $\mu_1, \mu_2$  are both real and negative with  $\mu_1\mu_2 = 1$ . The form of general solution is:

$$X(\tau) = c_1 e^{(\xi + \frac{1}{2}i)\tau} P_1(\tau) + c_2 e^{(-\xi + \frac{1}{2}i)\tau} P_2(\tau). \quad (\text{A } 14)$$

Here,  $e^{\xi\tau}$  leads to the exponential growth of solution and eventually becomes **unstable**, with **sub-harmonic** response. When  $-2 < \phi < +2$ :  $\mu_1, \mu_2$  are complex, we have  $\sigma_1 = i\zeta$  and  $\sigma_2 = -i\zeta$ , where  $\zeta$  is real, signifying that the solutions are bounded at all times and oscillatory but not necessarily periodic, and lies in **stable parameter region**. When  $\phi = +2$ :  $\mu_1 = \mu_2 = 1$ , one solution is periodic with period  $2\pi$  and lies on the **harmonic tongue of stability curve**  $\phi = 2$ . When  $\phi = -2$ :  $\mu_1 = \mu_2 = -1$ , one solution is periodic with period  $4\pi$  and lies on the **sub-harmonic tongue of stability curve**  $\phi = 2$ .

## REFERENCES

- AMIROUDINE, SAKIR, ZOUESHTIAGH, FARZAM & NARAYANAN, RANGA 2012 Mixing generated by faraday instability between miscible liquids. *Physical review E* **85** (1), 016326.
- ANDREWS, MALCOLM J & SPALDING, DUDLEY BRIAN 1990 A simple experiment to investigate two-dimensional mixing by rayleigh-taylor instability. *Physics of Fluids A: Fluid Dynamics* **2** (6), 922–927.
- BRIARD, ANTOINE, GOSTIAUX, LOUIS & GRÉA, BENOÎT-JOSEPH 2020 The turbulent faraday instability in miscible fluids. *Journal of Fluid Mechanics* **883**.
- BRIARD, ANTOINE, GRÉA, BENOÎT-JOSEPH & GOSTIAUX, LOUIS 2019 Harmonic to subharmonic transition of the faraday instability in miscible fluids. *Physical Review Fluids* **4** (4), 044502.
- BRUCKER, KYLE A & SARKAR, SUTANU 2010 A comparative study of self-propelled and towed wakes in a stratified fluid. *Journal of Fluid Mechanics* **652**, 373–404.
- CAVELIER, M, GRÉA, B-J, BRIARD, A & GOSTIAUX, L 2022 The subcritical transition to turbulence of faraday waves in miscible fluids. *Journal of Fluid Mechanics* **934**.
- CHALAMALLA, VAMSI K & SARKAR, SUTANU 2015 Mixing, dissipation rate, and their overturn-based estimates in a near-bottom turbulent flow driven by internal tides. *Journal of Physical Oceanography* **45** (8), 1969–1987.
- DIWAKAR, SV, ZOUESHTIAGH, FARZAM, AMIROUDINE, SAKIR & NARAYANAN, RANGA 2015 The faraday instability in miscible fluid systems. *Physics of Fluids* **27** (8), 084111.
- FARADAY, MICHAEL 1831 xvii. on a peculiar class of acoustical figures; and on certain forms assumed by

- groups of particles upon vibrating elastic surfaces. *Philosophical transactions of the Royal Society of London* (121), 299–340.
- FERNANDO, HARINDRA JS 1991 Turbulent mixing in stratified fluids. *Annual review of fluid mechanics* **23** (1), 455–493.
- FLEURY, M, MORY, M, HOPFINGER, EJ & AUCHERE, D 1991 Effects of rotation on turbulent mixing across a density interface. *Journal of Fluid Mechanics* **223**, 165–191.
- GRÉA, B-J & ADOU, A EBO 2018 What is the final size of turbulent mixing zones driven by the faraday instability?. *Journal of Fluid Mechanics* **837**, 293–319.
- GREGG, MICHAEL C, D'ASARO, ERIC A, RILEY, JAMES J & KUNZE, ERIC 2018 Mixing efficiency in the ocean. *Annual review of marine science* **10**, 443–473.
- JORDAN, DOMINIC & SMITH, PETER 2007 *Nonlinear ordinary differential equations: an introduction for scientists and engineers*. OUP Oxford.
- NASKAR, SOUVIK & PAL, ANIKESH 2022a Direct numerical simulations of optimal thermal convection in rotating plane layer dynamos. *Journal of Fluid Mechanics* **942**.
- NASKAR, SOUVIK & PAL, ANIKESH 2022b Effects of kinematic and magnetic boundary conditions on the dynamics of convection-driven plane layer dynamos. *Journal of Fluid Mechanics* **951**, A7.
- NIKURASHIN, MAXIM, VALLIS, GEOFFREY K & ADCROFT, ALISTAIR 2013 Routes to energy dissipation for geostrophic flows in the southern ocean. *Nature Geoscience* **6** (1), 48–51.
- NOH, YIGN & LONG, ROBERT R 1990 Turbulent mixing in a rotating, stratified fluid. *Geophysical & Astrophysical Fluid Dynamics* **53** (3), 125–143.
- PAL, ANIKESH 2020 Deep learning emulation of subgrid-scale processes in turbulent shear flows. *Geophysical Research Letters* **47** (12), e2020GL087005.
- PAL, ANIKESH & CHALAMALLA, VAMSI K 2020 Evolution of plumes and turbulent dynamics in deep-ocean convection. *Journal of Fluid Mechanics* **889**.
- PAL, ANIKESH & SARKAR, SUTANU 2015 Effect of external turbulence on the evolution of a wake in stratified and unstratified environments. *Journal of Fluid Mechanics* **772**, 361–385.
- PAL, ANIKESH, DE STADLER, MATTHEW B & SARKAR, SUTANU 2013 The spatial evolution of fluctuations in a self-propelled wake compared to a patch of turbulence. *Physics of Fluids* **25** (9), 095106.
- PELTIER, WR & CAULFIELD, CP 2003 Mixing efficiency in stratified shear flows. *Annual review of fluid mechanics* **35** (1), 135–167.
- ROSENBERG, DUANE, POUQUET, ANNICK, MARINO, RAFFAELE & MININNI, PABLO DANIEL 2015 Evidence for bolgiano-obukhov scaling in rotating stratified turbulence using high-resolution direct numerical simulations. *Physics of Fluids* **27** (5), 055105.
- SINGH, NARINDER & PAL, ANIKESH 2022 The onset and saturation of the faraday instability in miscible fluids in a rotating environment. *arXiv preprint arXiv:2207.13739*.
- TALLEY, LD, FEELY, RA, SLOYAN, BM, WANNINKHOF, R, BARINGER, MO, BULLISTER, JL, CARLSON, CA, DONEY, SC, FINE, RA, FIRING, E & OTHERS 2016 Changes in ocean heat, carbon content, and ventilation: a review of the first decade of go-ship global repeat hydrography. *Annual review of marine science* **8**, 185–215.
- WINTERS, KRAIG B & BARKAN, ROY 2013 Available potential energy density for boussinesq fluid flow. *Journal of Fluid Mechanics* **714**, 476–488.
- WINTERS, KRAIG B, LOMBARD, PETER N, RILEY, JAMES J & D'ASARO, ERIC A 1995 Available potential energy and mixing in density-stratified fluids. *Journal of Fluid Mechanics* **289**, 115–128.
- WUNSCH, CARL & FERRARI, RAFFAELE 2004 Vertical mixing, energy, and the general circulation of the oceans. *Annu. Rev. Fluid Mech.* **36**, 281–314.
- ZOUESHTIAGH, F, AMIROUDINE, S & NARAYANAN, R 2009 Experimental and numerical study of miscible faraday instability. *Journal of fluid mechanics* **628**, 43–55.